

ARTICLE

Received 10 Jul 2014 | Accepted 3 Nov 2014 | Published 10 Dec 2014

DOI: 10.1038/ncomms6745

All-organic optoelectronic sensor for pulse oximetry

Claire M. Lochner^{1,*}, Yasser Khan^{1,*}, Adrien Pierre^{1,*} & Ana C. Arias¹

Pulse oximetry is a ubiquitous non-invasive medical sensing method for measuring pulse rate and arterial blood oxygenation. Conventional pulse oximeters use expensive optoelectronic components that restrict sensing locations to finger tips or ear lobes due to their rigid form and area-scaling complexity. In this work, we report a pulse oximeter sensor based on organic materials, which are compatible with flexible substrates. Green (532 nm) and red (626 nm) organic light-emitting diodes (OLEDs) are used with an organic photodiode (OPD) sensitive at the aforementioned wavelengths. The sensor's active layers are deposited from solution-processed materials via spin-coating and printing techniques. The all-organic optoelectronic oximeter sensor is interfaced with conventional electronics at 1 kHz and the acquired pulse rate and oxygenation are calibrated and compared with a commercially available oximeter. The organic sensor accurately measures pulse rate and oxygenation with errors of 1% and 2%, respectively.

¹Department of Electrical Engineering and Computer Sciences, University of California, Berkeley, California 94720, USA. * These authors contributed equally to this work. Correspondence and requests for materials should be addressed to A.C.A. (email: acarias@eecs.berkeley.edu).

Conventional pulse oximeters non-invasively measure human pulse rate and arterial blood oxygen saturation with an optoelectronic sensor composed of two inorganic light-emitting diodes (LEDs) with different peak emission wavelengths and a single inorganic photodiode^{1,2}. The LEDs are placed on one side of a finger and the light transmitted through the tissue is subsequently sensed by the photodiode that is placed on the opposite side of the finger. Sequential sampling of the transmitted light provides information on the ratio of oxygenated and deoxygenated haemoglobin in the blood. This ratio and a calibration curve are used to compute arterial blood oxygen saturation. Currently, the application of commercially available pulse oximeters is limited by the bulk, rigidity and high large-area scaling cost of conventional inorganic-based optoelectronics. Here we show a pulse oximeter sensor composed of organic LEDs (OLEDs)^{3,4} and a flexible organic polymer photodiode (OPD)⁵. We successfully demonstrate that the organic optoelectronic sensor provides accurate measurement capability and we anticipate that our application of solution-processable organic optoelectronics in pulse oximetry will enable low-cost, disposable and wearable medical devices.

Wearable medical sensors have the potential to play an essential role in the reduction of health care costs: they encourage healthy living by providing individuals feedback on personal vital signs and enable the facile implementation of both in-hospital and in-home professional health monitoring. Consequently, wide implementation of these sensors can reduce prolonged hospital stays and cut avertible costs⁶. Recent reports show ample wearable sensors capable of measuring pressure^{7,8}, biopotential and bioimpedance^{9,10}, pulse rate¹¹ and temperature^{12,13} in real time. These sensors are developed in wearable and flexible form factors using organic^{8,13,14}, inorganic^{12,15,16} and hybrid organic-inorganic^{7,9,15} materials.

Organic semiconductors developed for OLEDs and OPDs have been primarily applied to display and photovoltaic technologies^{17,18}. This is due to their potential for large-area roll-to-roll manufacturing at large volumes, which is enabled by solution processing and the use of flexible substrates¹⁹. These attributes also make organic optoelectronics very attractive for medical sensors, where flexibility combined with large areas can result in an improvement of the overall sensor performance. In the past 10 years, a lot of resources were used to improve the stability of organic semiconductors to meet the lifetime requirements of displays and photovoltaics^{20,21}. When compared with the above markets, disposable medical sensors have less-stringent lifetime requirements on the materials, since these devices would be used only for a few days as opposed to years. Indeed, organic optoelectronics have previously been used to perform pulse measurements^{22–24}.

Here we report a sensor composed solely of organic optoelectronics that measures both human pulse and arterial blood oxygenation. We anticipate that our results will inspire system-level integration of organic-inorganic electronics, where the large area, low cost and mechanical flexibility of organic sensors will be combined with the computational efficiency of inorganic electronics. A schematic view of the sensor is given in Fig. 1a, where two OLED arrays and two OPDs are placed on opposite sides of a finger.

Results

Pulse and oxygenation with red and green organic light emitting diodes. In contrast to commercially available inorganic oximetry sensors, which use red and near-infrared LEDs, we use red and green OLEDs. Incident light from the OLEDs is attenuated by pulsating arterial blood, non-pulsating arterial blood,

venous blood and other tissue as depicted in Fig. 1b. When sampled with the OPD, light absorption in the finger peaks in systole (the heart's contraction phase) due to large amount of fresh arterial blood. During diastole (the heart's relaxation phase), reverse flow of arterial blood to the heart chambers reduces blood volume in the sensing location, which results in a minima in light absorption. This continuous change in arterial blood volume translates to a pulsating signal—the human pulse. The d.c. signal resulting from the non-pulsating arterial blood, venous blood and tissue is subtracted from the pulsating signal to give the amount of light absorbed by the oxygenated and deoxygenated haemoglobin in the pulsating arterial blood. Oxy-haemoglobin (HbO₂) and deoxy-haemoglobin (Hb) have different absorptivities at red and green wavelengths, as highlighted on the absorptivity of oxygenated and deoxygenated haemoglobin plotted in Fig. 1c. The difference in the molar extinction coefficient of oxygenated and deoxygenated haemoglobin at the green wavelength is comparable to the difference at near-infrared wavelengths (800–1,000 nm) used in conventional pulse oximeters. In addition, solution-processable near-infrared OLED materials are not stable in air and show overall lower efficiencies^{25,26}. Thus, we elected to use green OLEDs instead of near-infrared OLEDs.

Using red and green OLEDs and an OPD sensitive at visible wavelengths (the OLEDs' emission spectra and the OPD's external quantum efficiency (EQE) as a function of incident light wavelength are plotted in Fig. 1d), blood oxygen saturation (SO₂) is quantified according to equation 1. Here, C_{HbO₂} and C_{Hb} are the concentrations of oxy-haemoglobin and deoxy-haemoglobin, respectively.

$$SO_2 = \frac{C_{HbO_2}}{C_{HbO_2} + C_{Hb}} \quad (1)$$

R_{os}, the ratio of absorbed red (A_{rd}) and green (A_{gr}) light, depends on the normalized transmitted red (T_{n,rd}) and green (T_{n,gr}) light intensities according to Beer-Lambert's law (shown in equation 2).

$$R_{os} = \frac{A_{rd}}{A_{gr}} = \frac{\ln(T_{n,rd})}{\ln(T_{n,gr})} \quad (2)$$

Finally, arterial oxygen saturation (S_aO₂) can be calculated using equation 3. Here, ε_{rd,Hb} and ε_{gr,Hb} are the molar absorptivity of deoxy-haemoglobin at red (λ = 626 nm) and green (λ = 532 nm) wavelengths, respectively. Similarly, ε_{rd,HbO₂} and ε_{gr,HbO₂} are the molar absorptivity of oxy-haemoglobin at red (λ = 626 nm) and green (λ = 532 nm) wavelengths, respectively.

$$S_aO_2(R_{os}) = \frac{\epsilon_{rd,Hb} - \epsilon_{gr,Hb}R_{os}}{(\epsilon_{rd,Hb} - \epsilon_{rd,HbO_2}) + (\epsilon_{gr,HbO_2} - \epsilon_{gr,Hb})R_{os}} \quad (3)$$

Organic optoelectronic oximeter components. OLED and OPD performances are both paramount to the oximeter measurement quality. The most important performance parameters are the irradiance of the OLEDs' (Fig. 2b) and the EQE at short circuit of the OPD (Figs 1d and 3b). As the OLEDs operating voltage increases, irradiance increases at the expense of efficiency²⁷, as shown by the lower slope of irradiance than current as a function of applied voltage in Fig. 2b. For a pulse oximeter, this is an acceptable trade-off because higher irradiance from the OLEDs yields a strong measurement signal.

We have selected polyfluorene derivatives as the emissive layer in our OLEDs due to their environmental stability, relatively high efficiencies and self-assembling bulk heterojunctions that can be tuned to emit at different wavelengths of the light spectrum⁴. The green OLEDs were fabricated from a blend of poly(9,9-

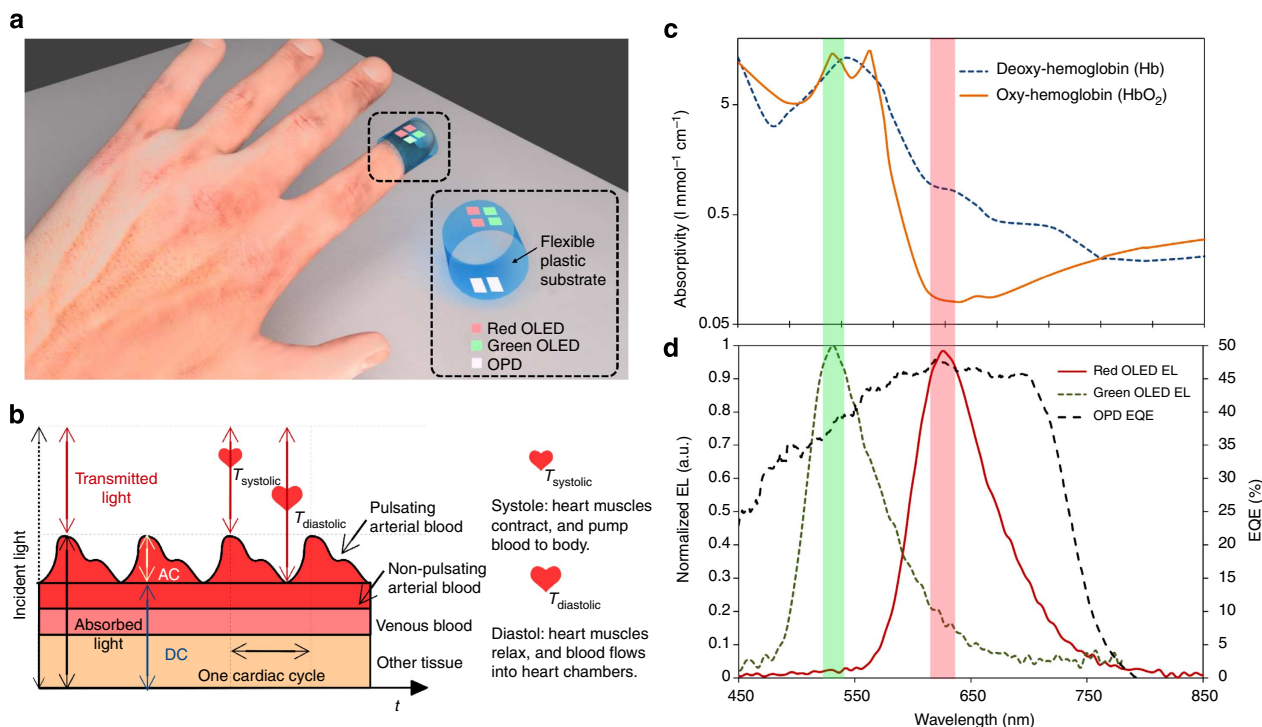


Figure 1 | Pulse oximetry with an organic optoelectronic sensor. (a) Pulse oximetry sensor composed of two OLED arrays and two OPDs. **(b)** A schematic illustration of a model for the pulse oximeter's light transmission path through pulsating arterial blood, non-pulsating arterial blood, venous blood and other tissues over several cardiac cycles. The a.c. and d.c. components of the blood and tissue are designated, as well as the peak and trough of transmitted light during diastole ($T_{\text{diastolic}}$) and systole (T_{systolic}), respectively. **(c)** Absorptivity of oxygenated (orange solid line) and deoxygenated (blue dashed line) haemoglobin in arterial blood as a function of wavelength. The wavelengths corresponding to the peak OLED electroluminescence (EL) spectra are highlighted to show that there is a difference in deoxy- and oxy-haemoglobin absorptivity at the wavelengths of interest. **(d)** OPD EQE (black dashed line) at short circuit, and EL spectra of red (red solid line) and green (green dashed line) OLEDs.

diocetylfluorene-*co*-*n*-(4-butylphenyl)-diphenylamine) (TFB) and poly((9,9-dioctylfluorene-2,7-diyl)-alt-(2,1,3-benzothiadiazole-4,8-diyl)) (F8BT). In these devices, electrons are injected into the F8BT phase of phase-separated bulk-heterojunction active layer while holes are injected into the TFB phase, forming excitons at the interfaces between the two phases and recombining in the lower energy F8BT phase for green emission²⁸. The emission spectrum of a representative device is shown in Fig. 1d. The red OLED was fabricated from a tri-blend blend of TFB, F8BT and poly((9,9-dioctylfluorene-2,7-diyl)-alt-(4,7-bis(3-hexylthiophene-5-yl)-2,1,3-benzothiadiazole)-2',2'-diyl)) (TBT) with an emission peak of 626 nm as shown in Fig. 1d. The energy structure of the full stack used in the fabrication of OLEDs, where ITO/PEDOT:PSS is used as the anode, TFB as an electron-blocking layer²⁹ and LiF/Al as the cathode, is shown in Fig. 2a. The physical structure of the device is provided in Supplementary Fig. 2b. The red OLED operates similarly to the green, with the additional step of excitonic transfer via Förster energy transfer³⁰ to the semiconductor with the lowest energy gap in the tri-blend, TBT, where radiative recombination occurs. The irradiance at 9 V for both types of OLEDs, green and red, was measured to be 20.1 and 5.83 mW cm⁻², respectively.

The ideal OPD for oximetry should exhibit stable operation under ambient conditions with high EQE at the peak OLED emission wavelengths (532 and 626 nm). A high EQE ensures the highest possible short-circuit current, from which the pulse and oxygenation values are derived. Poly({4,8-bis[(2-ethylhexyl)oxy]benzo[1,2-*b*:4,5-*b'*]dithiophene-2,6-diyl}{3-fluoro-2-[(2-ethylhexyl)carbonyl]thieno[3,4-*b*]thiophenediyl)) (PTB7) mixed with [6,6]-phenyl C71-butyric acid methyl ester (PC₇₁BM) is a stable donor:acceptor bulk-heterojunction OPD system, which yields

EQE as high as 80% for spin-coated devices⁵. The transparent electrode and active layer of the OPD are printed on a plastic substrate using a surface tension-assisted blade-coating technique recently developed and reported by Pierre *et al.*³¹ Figure 3a shows the energy band structure of our device including the transparent electrode (a high-conductivity/high-work-function PEDOT:PSS bilayer) and an Al cathode. The physical device structure of the OPD is shown in Supplementary Fig. 2d. The EQE at 532 and 626 nm is 38 and 47%, respectively, at short-circuit condition, as shown in Fig. 1d, and the leakage current of about 1 nA cm⁻² at 2 V applied reverse bias is shown in Fig. 3b together with the photocurrent when the device is illuminated with a 355 μW cm⁻² light source at 640 nm.

Despite the low reverse bias leakage current shown in Fig. 3b, we chose to bias the OPD at 0 V, the short-circuit condition, to sense low photocurrent levels. The frequency response of both the OPD and OLEDs was also characterized, since oximetry is usually performed at 1 kHz. The 3 dB cut-off was found to be at frequencies higher than 10 kHz for the all-organic optoelectronic sensor, which is significantly higher than the operational frequency required for oximetry (Supplementary Fig. 4). Notably, the frequency performance of the OPD is not hampered at short circuit because the shunt capacitance of organic photodiodes decreases negligibly with reverse bias, unlike inorganic photodiodes³².

We observed that the OLED irradiance for both red and green wavelengths is sufficient for the transmission of light through the finger and the signal acquired by the organic photodetector is sufficiently high for resolving the pulsating photoplethysmogram (PPG) signal shown in Fig. 1b. The pulse waveforms (two cardiac cycles) generated with a combination of organic and inorganic

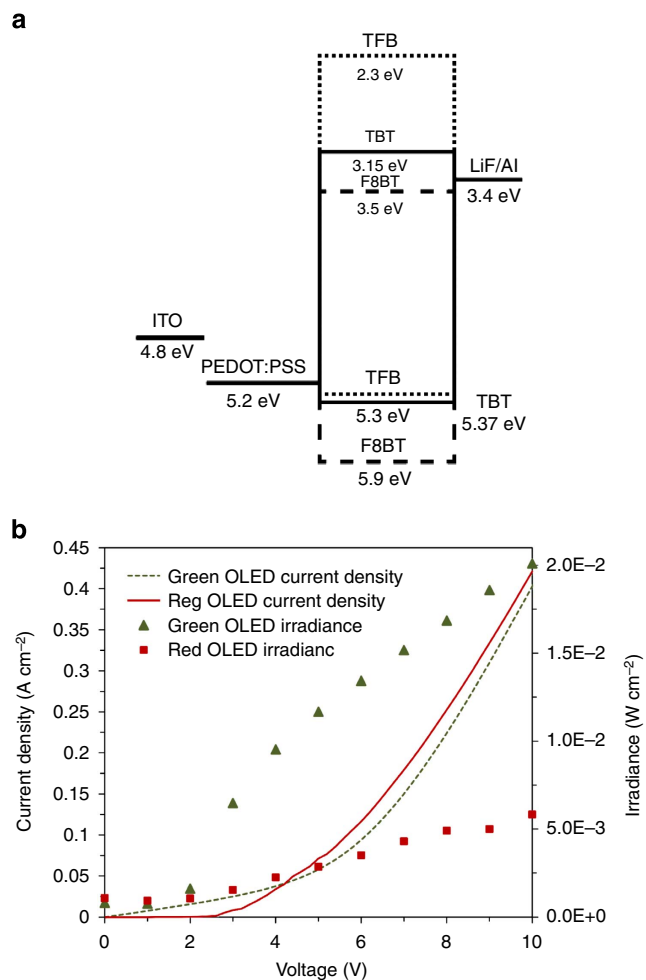


Figure 2 | OLED design and performance. (a) OLED energy structure. (b) Current density of red (red solid line) and green (green dashed line) OLEDs and irradiance of red (red squares) and green (green triangles) OLEDs as a function of applied voltage.

devices are shown in Fig. 4. The PPG obtained when a human finger is illuminated by inorganic LEDs and the transmitted light is measured with an OPD is shown in Fig. 4a. When the same measurement is performed using OLEDs and a conventional Si photodiode (Fig. 4b), the magnitude of the PPG signal is reduced from 26 to 16 mVp-p for the green and 16 to 6 mVp-p for the red due to the lower optical power of the organic LEDs compared with their inorganic equivalent device. Finally, both OLEDs and an OPD are used to obtain a PPG under the same experimental conditions (Fig. 4c), yielding signal magnitudes of 3 mVp-p for the green and 2.5 mVp-p for the red. It is clear that the magnitude of the signal is substantially reduced with the introduction of organic-based devices, but the PPG obtained at red and green wavelengths yields similar shapes for all device combinations shown in Fig. 4, which will result in similar pulse and arterial oxygenation values. The lower signal magnitude shown by the organic probe is compensated for by increasing the area of devices, resulting in higher photocurrents that directly translate into higher PPG signals, as shown in Supplementary Fig. 3a.

System design for an organic optoelectronic pulse oximeter.

The organic pulse oximetry sensor composed of two red and green OLED arrays and an OPD (Fig. 5a) is interfaced with a microcontroller that drives the OLEDs, measures the OPD signal

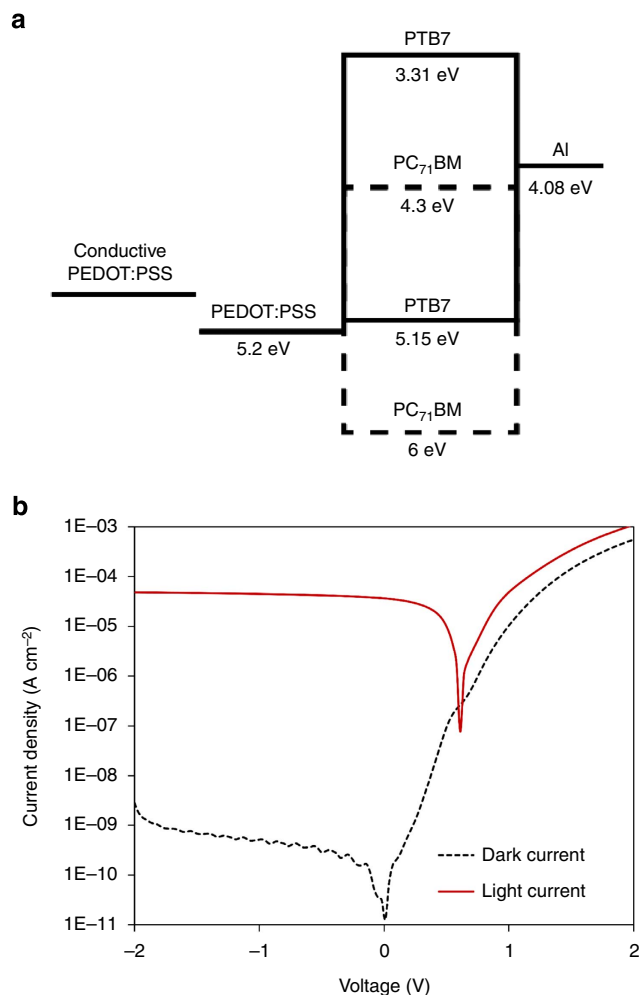


Figure 3 | OPD design and performance. (a) OPD energy structure. (b) Light current (red solid line) with excitation from a 640 nm, $355 \mu\text{W cm}^{-2}$ light source and dark current (black dashed line) as a function of applied voltage.

and transfers the data to a computer for analysis (Fig. 5b). The obtained signal from the OPD passes through an analogue front end where the PPG signal is filtered and amplified. The pulsating part of the signal yields heart rate and oxygenation according to an empirical correction to equation 3 (details are provided in Supplementary Methods and Supplementary Fig. 1). The accuracy of the organic optoelectronic sensor is characterized and calibrated by comparing pulse and oxygenation measurements taken simultaneously by the organic optoelectronic sensor and a commercially available pulse oximeter. The resultant pulse waveforms, pulse value, ratio of absorbed light and arterial blood oxygen saturation from the red and near-infrared LEDs in the inorganic oximeter and the red and green OLEDs in the organic oximeter are shown in Fig. 5c,d, respectively. The OLEDs are powered by a 9 V battery and the OPD is biased at 0 V. The a.c. component of the signal (Fig. 1b) is essential for visualizing cardiac rhythm and computing arterial blood oxygen saturation. The OPD read-out circuit consists of two internal operational amplifiers (Fig. 5b) in which the first stage amplifies the whole PPG signal from the photodiode. The second stage only amplifies the pulsating part of the signal and is read by an analogue-to-digital converter (ADC). With two-stage amplification, we obtained a 50–60 mVp-p PPG signal for the inorganic probe (Fig. 5c) and a 3–4 mVp-p PPG signal for the organic probe

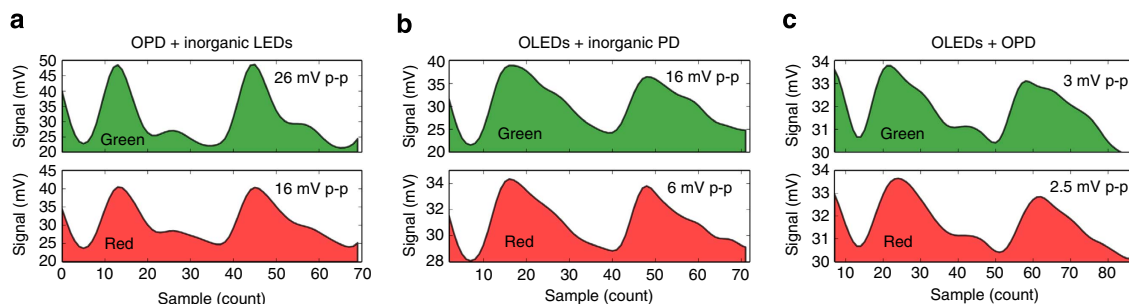


Figure 4 | PPG acquisition using combinations of inorganic and organic LEDs and photodiodes (PDs). (a) PPG signal acquired using inorganic red and green LEDs and an OPD. Green and red PPG signal amplitudes of 26 and 16 mVp-p were obtained, respectively. (b) PPG signal acquired using OLEDs and silicon PD—absence of lensing epoxy and reduced irradiance of the OLEDs bring down signal magnitude to 16 and 6 mVp-p for green and red excitations. (c) PPG signal acquired using OLEDs and OPD; although signal magnitudes are reduced to 3 and 2.5 mVp-p, the signal is sufficient for resolving the PPG waveform and provide light absorbance ratio information for arterial blood oxygenation calculation.

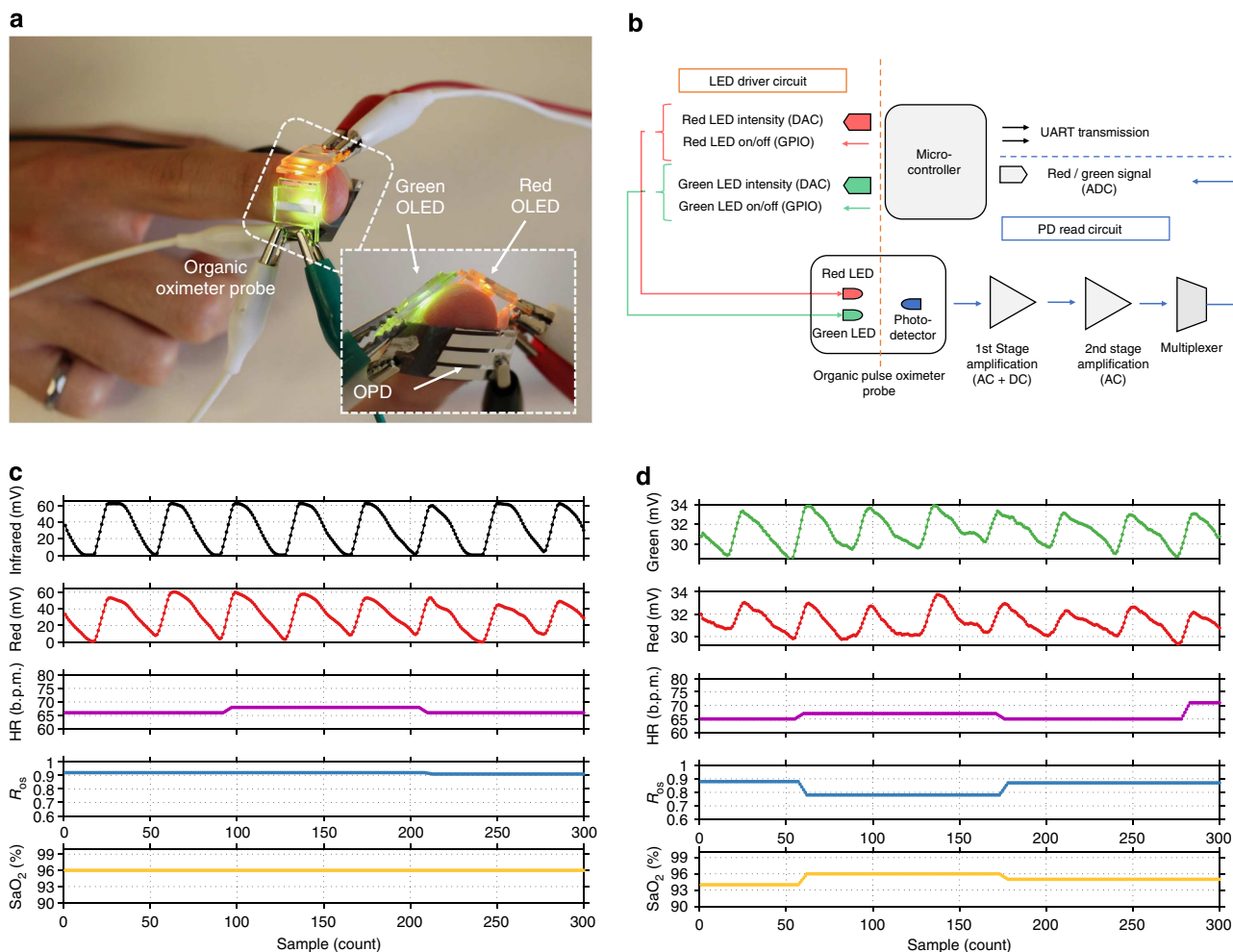


Figure 5 | Organic optoelectronic pulse oximetry system. (a) Red and green OLEDs are placed on subject’s finger and transmitted light is collected with one OPD pixel placed below the finger. (b) Hardware block diagram for the system set-up—a microcontroller acts as the data acquisition and processing unit. OLEDs are triggered and controlled using general-purpose input/output port and DAC pins, and the OPD signal is recorded using the ADC of the microcontroller. A two-stage amplifier between the OPD and ADC removes the d.c. part from the PPG signal and amplifies the pulsating PPG signal. (c,d) Simultaneous oximetry measurements with a commercially available inorganic oximeter probe and the organic oximeter probe, respectively. The PPG signal was obtained using red and infrared light for the commercially available probe (c) and using red and green light for the organic probe (d). Heart rate (HR; magenta line in c,d) was obtained by timing the systolic peaks in the PPG signals. The ratio of the transmitted light at two wavelengths (R_{os} ; blue line in c,d) is converted to arterial blood oxygen saturation (S_{aO_2} ; yellow line in c,d) using Beer-Lambert’s law in conjunction with an empirical correction.

(Fig. 5d). The heart rate and ratio of transmitted light at two wavelengths (Fig. 5c,d) were calculated directly from the PPG signals and the arterial blood oxygen saturation was derived from

the ratio of transmitted light, as discussed previously and in the Supplementary Methods. The calculated heart rate and oxygenation derived from the PPG signals from the inorganic and

organic probes are both 65–70 beats per minute and 94–96%, respectively (Fig. 5c,d). We observed 1% error for pulse rate and 2% error for oxygenation when comparing the organic optoelectronic sensor with the inorganic sensor.

Motion artefacts are one possible source of error in pulse oximetry measurements. Motion-induced errors can be minimized with signal-processing algorithms that can be found in literature^{33,34}. In this work, we focus mainly on organic optoelectronic probe design and development; motion artefact characterization and mitigation algorithms can be implemented to further improve sensor performance.

Discussion

The novel combination of red and green OLEDs, as opposed to a red and near-infrared LED pair, is successfully implemented in pulse oximetry because the difference in the absorptivity of oxygenated and deoxygenated haemoglobin at the green wavelength is comparable to the difference at near-infrared wavelengths³⁵ as seen in Fig. 1c. Green LEDs have not been used conventionally in transmission oximetry because shorter wavelengths are more efficiently absorbed by the blood. However, the higher irradiance of the green OLEDs (Fig. 2b) compensates for any absorption losses in non-pulsating blood and tissue, as can be inferred from the higher green signal amplitudes in Fig. 4 compared with the red signal amplitudes. We employed an empirical correction to calculate arterial blood oxygenation from the ratio of transmitted green and red light, a scheme widely used for correcting for the deviation from Beer–Lambert's law (which does not account for the scattering that occurs in human tissue) in red and near-infrared pulse oximetry measurements.

Aside from maximizing OPD EQE and short-circuit photocurrent and OLED irradiance, the OPD's short-circuit current resulting from ambient light should be minimized to achieve the best pulse oximetry signal, as parasitic photodetector current is a contributor to conventional pulse oximetry failure³⁶. The effects of ambient light on the OPD's short-circuit current were measured using two-finger phantoms with radii of 9 and 5 mm, representative of the wide range of human finger sizes. Flexing the photodiode around the finger phantom, as opposed to taking the measurement with the photodiode placed flat, non-flexed, against the phantom, significantly reduces the parasitic short-circuit current produced by ambient light. Under typical room-lighting conditions of 72–76 $\mu\text{W cm}^{-2}$, flexing the OPD around the 9 and 5 mm radii phantoms reduced the parasitic current from 270 to 20 nA and 280 to 60 nA, respectively (Supplementary Fig. 3b). The ability of the flexible OPD to conform around the human body therefore improves the pulse oximeter's versatility.

The long-term stability of the organic optoelectronic pulse oximeter, like most organic optoelectronics, is limited by the robustness of the encapsulation technology employed in its fabrication^{37,38}. It has been shown that lifetime of organic optoelectronics can be significantly improved using robust encapsulation and packaging. With our encapsulation process, we see a 24% signal intensity decrease in the green and a 54% decrease in the red PPG signal over a 7-day time frame. Supplementary Figure 5 shows a decline in signal intensity; however, the PPG signal shapes are intact.

The organic optoelectronic pulse oximetry sensor described here demonstrates the potential for the application of organic electronics to thrive in the medical device field. The large-area scalability, inexpensive processing and flexibility of organic optoelectronics will allow medical sensors to be made in new shapes and sizes, diversifying possible sensing locations on the human body, enabling medical professionals to better monitor their patients' care.

Methods

OLED fabrication and characterization. The semiconducting polymers used in the emissive layer of the OLEDs were supplied by Cambridge Display Technology Limited. The red OLED active layer was made from a 25:70:5 blend of TFB:F8BT:TBT in a 10 mg ml⁻¹ *o*-xylene solution. The green OLED active layer was made from a 1:9 blend of TFB:F8BT in a 10 mg ml⁻¹ *o*-xylene solution. Patterned ITO substrates were cleaned via sonication in acetone and then isopropyl alcohol. The substrate surfaces were made hydrophilic with a 2 min plasma treatment before spincoating a 40 nm layer of Clevis PEDOT:PSS AI4083. Any remaining moisture was evaporated in a 10 min annealing step at 120 °C before moving the samples into a nitrogen glove box for the remainder of the fabrication procedure. TFB was spin coated from a 10 mg ml⁻¹ *o*-xylene solution and then annealed at 180 °C for 45 min before cooling and spin rinsing with *o*-xylene, producing a 10–20 nm-thick electron-blocking layer. The active layer was then spun at 4500 r.p.m. for a 100 nm film thickness. The LiF (1 nm)/Al (100 nm) cathode was thermally evaporated under vacuum at 4×10^{-6} Torr. Finished devices were encapsulated with ultraviolet-curable Delo Katiobond LP612 epoxy and clean quartz glass. Each OLED pixel had 4 mm² of active area. OLED current/voltage characteristics and irradiance measurements were taken with an Orb Optronix light measurement system complete with an Orb Optronix SP-50 spectrometer, integrating sphere, Keithley 2400 Source Meter and Spectral Suite 3.0 software.

OPD fabrication and characterization. OPDs were printed on top of planarized polyethylene naphthalate (PEN) substrates (DuPont) using a blade-coating technique previously reported³¹. A layer of high-conductivity PEDOT:PSS (Sigma-Aldrich, 739316-25G) was printed by blade coating (200 μm blade height at 1.6 cm s⁻¹) the solution over a large hydrophilic strip in the substrate defined by a 10 s plasma treatment through a stencil. Following a 10 min anneal at 120 °C, a layer of high-work-function PEDOT:PSS (Clevis AI4083) was coated and annealed over the previous print using the same process. The active layer ink comprised of a 1:1 weight ratio of PTB7:PC₇₁BM (Solaris Chem) dissolved to 35 mg ml⁻¹ in chlorobenzene with a 3 vol.% concentration of 1,8-diiodooctane and was blade coated (350 μm blade height at 1.6 cm s⁻¹) in a glove box with the substrate heated to 40 °C. The aluminum cathode (100 nm) was thermally evaporated under vacuum at 4×10^{-6} Torr to yield an active area of 21 mm². Finished devices were encapsulated with ultraviolet-curable Delo Katiobond LP612 epoxy and Saran wrap after being post-annealed at 120 °C for 10 min. All OLED and OPD layer thicknesses were measured with a Dektak Profilometer.

Electronic hardware and software for data acquisition and processing. The Texas Instruments MSP430 microcontroller was chosen for data acquisition and processing because of its built-in ADCs and digital-to-analogue converters (DACs), which are required for the pulse oximeter. General-purpose input–output pins from the microcontroller control LED switching, ADCs are utilized to read the amplified OPD signal from the multiplexer, and DACs are used to control LED intensity and in the signal amplification stage. The LEDs are operated in a sequential approach, so that only one of the LEDs is on at a particular moment. Five hundred and twelve samples are taken from each of the LEDs per second. A software trigger from the microcontroller controls a PNP bipolar junction transistor (BJT) switch that triggers the LED on/off. In addition, DACs are used to control the drive current for the LEDs using a NPN transistor. For ensuring compatibility with the organic LEDs, signals from the microcontroller are shifted to 9 V using general-purpose operational amplifiers. Finally, universal asynchronous receiver/transmitter (UART) protocol is used to send processed data to a computer for visualization. We opted for a modular approach by separating the LED driver circuit and OPD read circuit, simplifying circuit design and debugging. Hamamatsu Large Area Photodiode S1227-1010BQ (active area of 35 mm²) and 5 mm red and green round LEDs were used in PPG data comparisons with the organic devices.

All-pulse oximetry experiments performed on human subjects were carried out with informed consent under the approval of the University of California, Berkeley Institutional Review Board, protocol ID number 2013-03-6081.

References

1. Yelderman, M. & New, Jr W. Evaluation of pulse oximetry. *Anesthesiology* **59**, 349–351 (1983).
2. Webster, J. G. *Design of Pulse Oximeters, Series in Medical Physics and Biomedical Engineering* (Taylor & Francis, 2002).
3. Burroughes, J. H. *et al.* Light-emitting diodes based on conjugated polymers. *Nature* **347**, 539–541 (1990).
4. Morteani, A. C. *et al.* Barrier-free electronhole capture in polymer blend heterojunction light-emitting diodes. *Adv. Mater.* **15**, 1708–1712 (2003).
5. He, Z. *et al.* Enhanced power-conversion efficiency in polymer solar cells using an inverted device structure. *Nat. Photon.* **6**, 591–595 (2012).
6. Penders, J. *et al.* *VLSI-SoC: Research Trends in VLSI and Systems on Chip* 377–397 (Springer, 2008).

7. Pan, L. *et al.* An ultra-sensitive resistive pressure sensor based on hollow-sphere microstructure induced elasticity in conducting polymer film. *Nat. Commun.* **5**, 3002 (2014).
8. Schwartz, G. *et al.* Flexible polymer transistors with high pressure sensitivity for application in electronic skin and health monitoring. *Nat. Commun.* **4**, 1859 (2013).
9. Xu, S. *et al.* Soft mi-crofluidic assemblies of sensors, circuits, and radios for the skin. *Science* **344**, 70–74 (2014).
10. Jeong, G. S. *et al.* Solderable and electroplatable flexible electronic circuit on a porous stretchable elastomer. *Nat. Commun.* **3**, 977 (2012).
11. Mendelson, Y., Duckworth, R. J. & Comtois, G. in *Engineering in Medicine and Biology Society, 2006. EMBS'06. 28th Annual International Conference of the IEEE* 912–915 (IEEE, 2006).
12. Jeon, J., Lee, H. B. & Bao, Z. Flexible wireless temperature sensors based on ni microparticle-filled binary polymer composites. *Adv. Mater.* **25**, 850–855 (2013).
13. Someya, T. *et al.* Conformable, flexible, large-area networks of pressure and thermal sensors with organic transistor active matrixes. *Proc. Natl Acad. Sci. USA* **102**, 12321–12325 (2005).
14. Sekitani, T., Zschieschang, U., Klauk, H. & Someya, T. Flexible organic transistors and circuits with extreme bending stability. *Nat. Mater.* **9**, 1015–1022 (2010).
15. Donghee, S. *et al.* Multifunctional wearable devices for diagnosis and therapy of movement disorders. *Nat. Nanotechnol.* **9**, 397–404 (2014).
16. Sun, Y. & Rogers, J. A. Inorganic semiconductors for flexible electronics. *Adv. Mater.* **19**, 1897–1916 (2007).
17. Ma, R.-Q. *et al.* Flexible active-matrix oled displays: challenges and progress. *J. Soc. Inf. Disp.* **16**, 169–175 (2008).
18. Tang, C. W. Two-layer organic photovoltaic cell. *Appl. Phys. Lett.* **48**, 183–185 (1986).
19. Williams, G., Backhouse, C. & Aziz, H. Integration of organic light emitting diodes and organic photodetectors for lab-on-a-chip bio-detection systems. *Electronics* **3**, 43–75 (2014).
20. Kreyenschmidt, M. *et al.* Thermally stable blue-light-emitting copoly-mers of poly(alkylfluorene). *Macromolecules* **31**, 1099–1103 (1998).
21. Peters, C. H. *et al.* The mechanism of burn-in loss in a high efficiency polymer solar cell. *Adv. Mater.* **24**, 663–668 (2012).
22. Koetse, M. *et al.* in *Photonic Devices + Applications* (International Society for Optics and Photonics, 2008).
23. Koetse, M. M. *et al.* in *Sensors Applications Symposium, 2008. SAS 2008. IEEE* 1–3 (IET, 2008).
24. Chuo, Y., Omrane, B., Landrock, C., Patel, J. N. & Kaminska, B. Platform for all-polymer-based pulse-oximetry sensor. *Sensors 2010 IEEE* 155–159 (2010).
25. Caspar, J. V., Kober, E. M., Sullivan, B. P. & Meyer, T. J. Application of the energy gap law to the decay of charge-transfer excited states. *J. Am. Chem. Soc.* **104**, 630–632 (1982).
26. Sommer, J. R. *et al.* Efficient near-infrared polymer and organic light-emitting diodes based on electrophosphorescence from (tetraphenyltetranaphtho [2, 3] porphyrin) platinum (ii). *ACS Appl. Mater. Interfaces* **1**, 274–278 (2009).
27. Forrest, S. R., Bradley, D. D. C. & Thompson, M. E. Measuring the efficiency of organic light-emitting devices. *Adv. Mater.* **15**, 1043–1048 (2003).
28. Kim, J.-S. *et al.* Optoelectronic and charge transport properties at organic-organic semiconductor interfaces: comparison between polyfluorene-based polymer blend and copolymer. *J. Am. Chem. Soc.* **130**, 13120–13131 (2008).
29. Kim, J.-S., Friend, R. H., Grizzi, I. & Burroughes, J. H. Spin-cast thin semiconducting polymer interlayer for improving device efficiency of polymer light-emitting diodes. *Appl. Phys. Lett.* **87**, 023506 (2005).
30. Forster, Th. 10th spiers memorial lecture. Transfer mechanisms of electronic excitation. *Discuss. Faraday Soc.* **27**, 7–17 (1959).
31. Pierre, A. *et al.* All-printed flexible organic transistors enabled by surface tension-guided blade coating. *Adv. Mater.* **26**, 5722–5727 (2014).
32. Yao, Y. *et al.* Plastic near-infrared photodetectors utilizing low band gap polymer. *Adv. Mater.* **19**, 3979–3983 (2007).
33. Goldman, J. M., Petterson, M. T., Kopotic, R. J. & Barker, S. J. Masimo signal extraction pulse oximetry. *J. Clin. Monit. Comput.* **16**, 475–483 (2000).
34. Yousefi, R., Nourani, M., Ostadabbas, S. & Panahi, I. A motion-tolerant adaptive algorithm for wearable photoplethysmographic biosensors. *IEEE J. Biomed. Health Inform.* **18**, 670–681 (2014).
35. Zijlstra, W. G., Buursma, A. & Meeuwse-Van der Roest, W. P. Absorption spectra of human fetal and adult oxyhemoglobin, de-oxyhemoglobin, carboxyhemoglobin, and methemoglobin. *Clin. Chem.* **37**, 1633–1638 (1991).
36. Trivedi, N. S., Ghouri, A. F., Shah, N. K., Lai, E. & Barker, S. J. Effects of motion, ambient light, and hypoperfusion on pulse oximeter function. *J. Clin. Anesth.* **9**, 179–183 (1997).
37. Ahmad, J., Bazaka, K., Anderson, L. J., White, R. D. & Jacob, M. V. Materials and methods for encapsulation of opv: a review. *Renew. Sustain. Energy Rev.* **27**, 104–117 (2013).
38. Park, J.-S., Chae, H., Chung, H. K. & Lee, S. I. Thin film encapsulation for flexible am-oled: a review. *Semicond. Sci. Technol.* **26**, 034001 (2011).

Acknowledgements

This work was supported in part by the National Science Foundation under Cooperative Agreements No. ECCS-1202189 and UTA-12000944, ARL W911NF-09-3-001 under RFP 12-159 and by the NSF Graduate Fellowship Research Program under Grant No. DGE-1106400. We thank Cambridge Display Technology Limited (CDT) for supplying OLED materials, and Dr Mozziyar Etemadi for helpful technical discussions.

Author contributions

A.C.A., C.M.L., A.P. and Y.K. conceptualized the work. C.M.L. and A.P. carried out device fabrication and characterization of the OLEDs and OPDs, respectively, and experimental set-ups. Y.K. designed and implemented the oximeter system and worked on software and hardware programming. C.M.L., A.P. and Y.K. volunteered as subjects and collected pulse and oxygenation results. All authors discussed the results and commented on the manuscript.

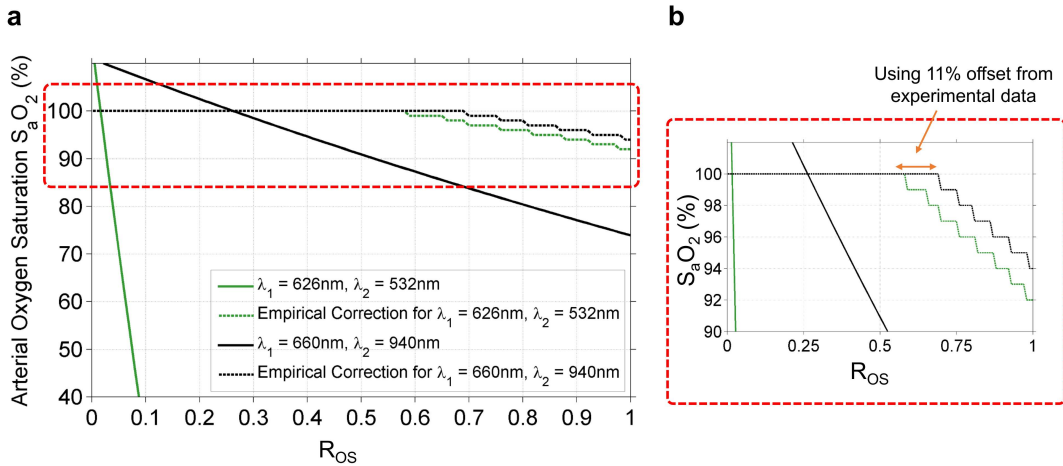
Additional information

Supplementary Information accompanies this paper at <http://www.nature.com/naturecommunications>

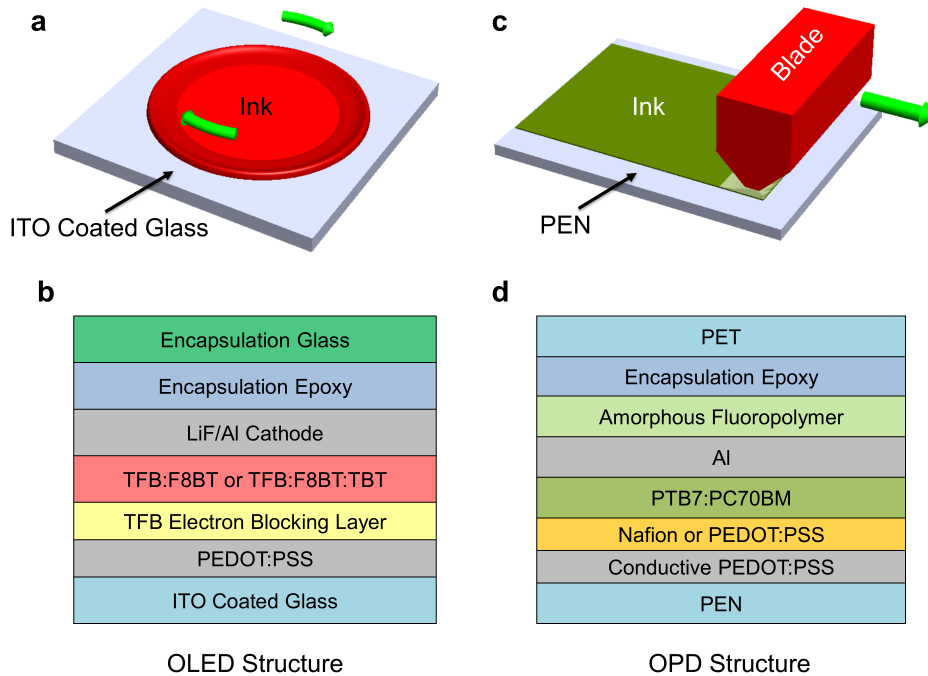
Competing financial interests: The authors declare no competing financial interests.

Reprints and permission information is available online at <http://npg.nature.com/reprintsandpermissions/>

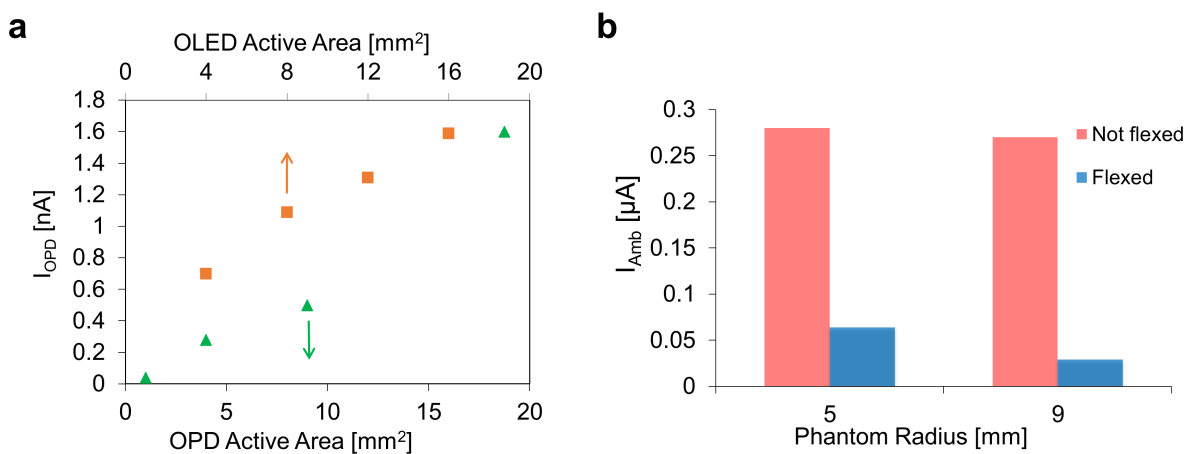
How to cite this article: Lochner, C. M. *et al.* All-organic optoelectronic sensor for pulse oximetry. *Nat. Commun.* 5:5745 doi: 10.1038/ncomms6745 (2014).



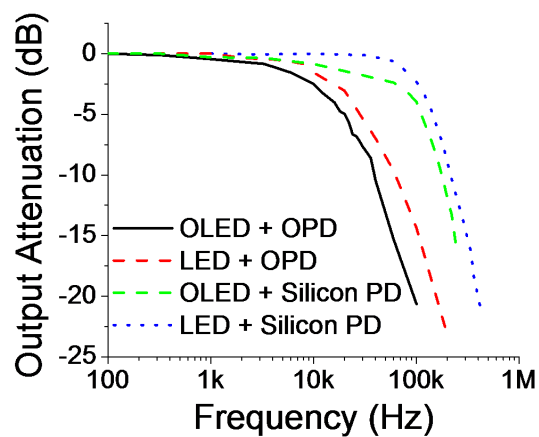
Supplementary Figure 1: **Arterial oxygen saturation (S_aO_2) as a function of transmitted light ratio (R_{OS}).** **a**, The **black solid line** shows the curve generated by Beer-Lambert's Law for red ($\lambda = 660$ nm) and infrared ($\lambda = 940$ nm) light. Similarly, the **green solid line** shows the curve generated by Beer-Lambert's Law for red ($\lambda = 626$ nm) and green ($\lambda = 532$ nm) light. Calibration curves to overcome limitations of Beer-Lambert's Law in scattering tissue (versus a glass cuvette) are shown by **dashed lines**. R_{OS} values were measured for various S_aO_2 values. **b**, We observed an 11% offset for the green light oximeter (**green dashed line**) from the conventional oximeter (**black dashed line**).



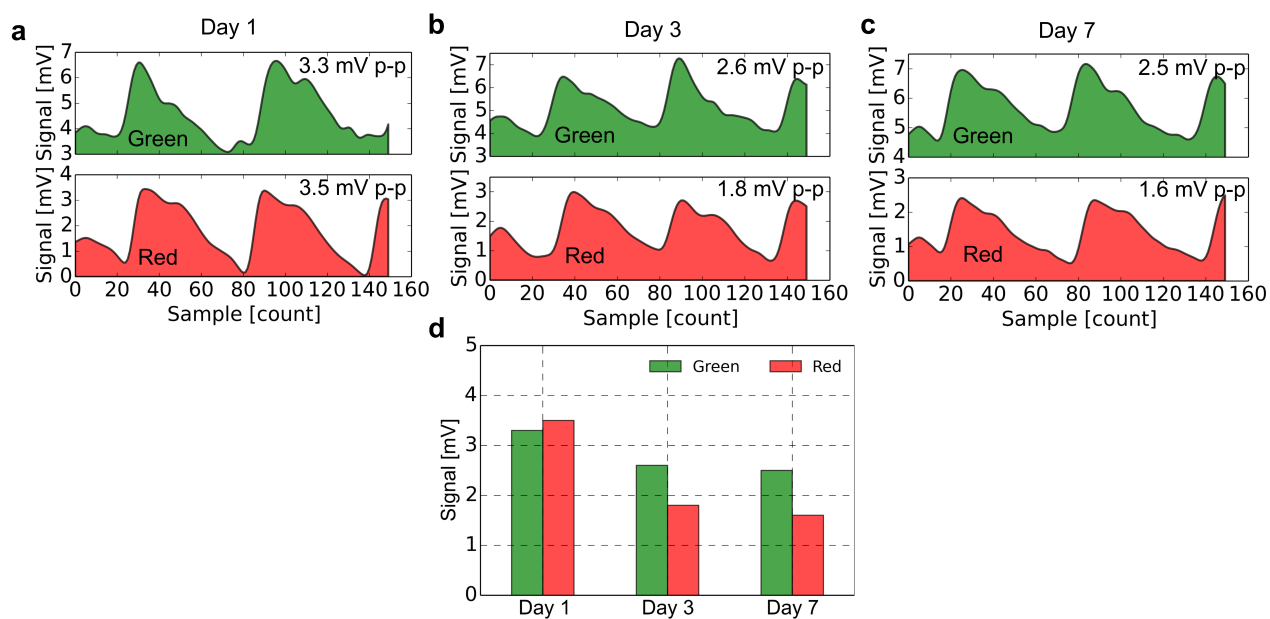
Supplementary Figure 2: **OLED and OPD fabrication and physical device structures.** **a**, The OLEDs are fabricated on a glass substrate using spin coating. **c**, The OPDs are fabricated using blade coating on a PEN substrate [4]. **b and d** respectively show the physical structures of the OLEDs and OPDs.



Supplementary Figure 3: **Area scaling effects of OLEDs and OPDs, and reducing ambient noise by flexing the OPD around a finger phantom.** **a**, OPD current (I_{OPD}) was observed for different OLED and OPD active areas. As expected, higher photo-current resulted with area scaling of the OLEDs and OPDs. **b**, OPDs were flexed around 5 mm and 9 mm radius phantoms representative of small and large human fingers. 79% and 93% reduction in ambient noise were observed for the OPDs flexed around the phantoms, respectively.



Supplementary Figure 4: **Frequency response of various organic and inorganic LED and PD configurations.** The inorganic LED and PD showed the best response with a 3dB cutoff greater than 100 kHz. For the all organic combination with OLED and OPD, 10 KHz cutoff was obtained, which is significantly higher than the 1 kHz operation of the oximeter. Green ($\lambda = 532$ nm) LEDs and OLEDs were used with a 5 V peak to peak sinusoidal signal and a DC offset of 2.5V.



Supplementary Figure 5: **Stability of the all-organic optoelectronic sensor.** **a**, **b**, and **c**, Recorded signal intensities on day 1, 3, and 7 respectively after fabrication of the sensor. **d** Bar chart showing the degradation in signal intensity over seven day time period. Decline in performance is mainly due to encapsulation failure of the organic optoelectronics [5, 6].

A. Pulse oximetry using red and green OLEDs

In contrast to commercially available inorganic oximetry sensors, which use red and near-infrared LEDs, we used red and green OLEDs. We have replaced the near-infrared LED with a green OLED due to fact that solution-processable near-infrared OLEDs suffer from lower efficiencies. This substitution did not affect the pulse oximetry measurements because the difference in the molar extinction coefficient of oxygenated and deoxygenated hemoglobin at the green wavelength is comparable to the difference at near-infrared wavelengths. Conventionally, the saturation of oxygen in blood (SO_2) is quantified from the concentration of oxygenated hemoglobin C_{HbO_2} and the concentration of deoxygenated hemoglobin C_{Hb} [1–3]:

$$SO_2 = \frac{C_{HbO_2}}{C_{HbO_2} + C_{Hb}} \quad (1)$$

In transmission mode pulse oximetry, light from LEDs is directed into the top of the finger and the transmitted light is sensed at the bottom of the finger with a photodetector. Beer-Lambert's law states that the intensity of light traveling through a medium decreases exponentially with distance. Transmission T is given by,

$$T = I_0 \exp(-\varepsilon Cd) \quad (2)$$

Here, I_0 is the incident light intensity, ε is the molar absorptivity with units of $L \text{ mM}^{-1} \text{ cm}^{-1}$, C is the concentration of the absorbent medium, and d is the optical path length through the medium.

The absorbance, A , is now defined as,

$$A = -\ln \frac{T}{I_0} = \varepsilon Cd \quad (3)$$

Now if we consider attenuation in skin, tissue, and bones – represented with the subscript DC , and attenuation in oxy-hemoglobin and deoxy-hemoglobin – represented with the subscripts HbO_2 and Hb , the following equations represent transmission at diastole and systole:

$$T_{high,dia} = I_0 \exp(-\varepsilon_{DC} C_{DC} d_{DC}) \exp(-(\varepsilon_{HbO_2} C_{HbO_2} + \varepsilon_{Hb} C_{Hb}) d_{dia}) \quad (4)$$

$$T_{low,sys} = I_0 \exp(-\varepsilon_{DC} C_{DC} d_{DC}) \exp(-(\varepsilon_{HbO_2} C_{HbO_2} + \varepsilon_{Hb} C_{Hb}) d_{sys}) \quad (5)$$

Light has to pass through the additional optical path Δd at systole, therefore $d_{sys} = d_{dia} + \Delta d$. Additionally, a normalization step ($T_{normalized} = T/T_{high,dia}$) is required to determine the normalized systolic transmission.

Now Eq. 3 can be rewritten by superpositioning absorbance of HbO_2 and HbO at a specific wavelength,

$$A = (\varepsilon_{HbO_2} S_a O_2 + \varepsilon_{Hb} (1 - S_a O_2)) (C_{HbO_2} + C_{Hb}) \Delta d \quad (6)$$

The ratio of the absorbance at red (rd) and green (gr) light can be found using the following equation,

$$R_{os} = \frac{A_{rd}}{A_{gr}} = \frac{(\varepsilon_{rd,HbO_2} S_a O_2 + \varepsilon_{rd,Hb} (1 - S_a O_2)) (C_{HbO_2} + C_{Hb}) \Delta d}{(\varepsilon_{gr,HbO_2} S_a O_2 + \varepsilon_{gr,Hb} (1 - S_a O_2)) (C_{HbO_2} + C_{Hb}) \Delta d} \quad (7)$$

Finally, arterial oxygen saturation ($S_a O_2$) can be calculated using Eq. 8. Here, $\varepsilon_{rd,Hb}$ and $\varepsilon_{gr,Hb}$ are the molar absorptivity of deoxy-hemoglobin at red ($\lambda = 626 \text{ nm}$) and green ($\lambda = 532 \text{ nm}$) wavelengths. Similarly, ε_{rd,HbO_2} and ε_{gr,HbO_2} are the molar absorptivity of oxy-hemoglobin at red ($\lambda = 626 \text{ nm}$) and green ($\lambda = 532 \text{ nm}$) wavelengths.

$$S_a O_2 (R_{os}) = \frac{\varepsilon_{rd,Hb} - \varepsilon_{gr,Hb} R_{os}}{(\varepsilon_{rd,Hb} - \varepsilon_{rd,HbO_2}) + (\varepsilon_{gr,HbO_2} - \varepsilon_{gr,Hb}) R_{os}} \quad (8)$$

$S_a O_2$ vs R_{os} for both red-infrared and red-green combinations are shown in Supplementary Figure 1a. However, empirical correction is required to overcome limitations of Beer-Lambert's Law in scattering tissue (versus a glass cuvette), which is given in Supplementary Figure 1b. We experimentally obtained the 11% offset in the calibration curves.

- [1] J. Webster, *Design of Pulse Oximeters*, Series in Medical Physics and Biomedical Engineering (Taylor & Francis, 2002), ISBN 9781420050790.
- [2] M. Yelderian and W. New Jr, *Anesthesiology* **59**, 349 (1983).
- [3] R. Haahr, M.S. thesis, Technical University of Denmark (2006).
- [4] A. Pierre, M. Sadeghi, M. M. Payne, A. Facchetti, J. E. Anthony, and A. C. Arias, *Advanced Materials* **26**, 5722 (2014).
- [5] J. Ahmad, K. Bazaka, L. J. Anderson, R. D. White, and M. V. Jacob, *Renewable and Sustainable Energy Reviews* **27**, 104 (2013).
- [6] J.-S. Park, H. Chae, H. K. Chung, and S. I. Lee, *Semiconductor Science and Technology* **26**, 034001 (2011).